Photothermal circular dichroism studies of single nanoparticles

Späth, P.R.

2

Circular dichroism measurement of single metal nanoparticles using photothermal imaging

Circular dichroism (CD) spectroscopy is a powerful optical technique for the study of chiral materials and molecules. It gives access to an enantioselective signal based on the differential absorption of right and left circularly polarized light, usually obtained through polarization analysis of the light transmitted through a sample of interest. CD is routinely used to determine the secondary structure of proteins and their conformational state. However, CD signals are weak, limiting the use of this powerful technique to ensembles of many molecules. Here, we experimentally realize the concept of photothermal circular dichroism, a technique that combines the enantioselective signal from circular dichroism with the high sensitivity of photothermal microscopy, achieving a superior signal-to-noise ratio to detect chiral nano-objects. As a proof of principle, we studied the chiral response of single plasmonic nanostructures with CD in the visible range, demonstrating a signal-to-noise ratio better than 40 with only $30\,\mathrm{ms}$ *integration time for these nanostructures. The high signal-to-noise ratio allows us to quantify the CD signal for individual nanoparticles. We show that we can distinguish relative absorption differences for right circularly and left circularly polarized light as small as* $g_{min} = 4 \times 10^{-3}$ *for a* $30\,\mathrm{ms}$ *integration time with our current experimental settings. The enhanced sensitivity of our technique extends CD studies to individual nano-objects and opens CD spectroscopy to numbers of molecules much lower than those in conventional experiments.*

This chapter is based on the publication in Nano Letters **19**, 12 (2019).

2.1. Introduction

An object is chiral when its mirror image cannot be superimposed with the original object [1, 2]. The most prominent examples of chirality are found at all scales in life, from whole organisms to biomolecules such as DNA, most sugars as well as amino-acids, which often occur only in one handedness [3, 4]. Chirality at the molecular level arises from the relative spatial arrangement of the constituent atoms in a molecule; the two mirror-symmetric isomers of a chiral molecule are called enantiomers. Despite their identical chemical composition, enantiomers can have dramatically different biological activities, metabolism rates and toxicities [5]. Therefore, methods for detecting molecular chirality and separating enantiomers are highly relevant for drug development. The standard optical technique to study chirality of biomolecules and biomacromolecules is circular dichroism (CD) spectroscopy [5–7], which gives access to the handedness of a molecule and also provides insight into the secondary structure and the conformational state of proteins [8, 9]. Circular dichroism measurements amount to detecting the differential absorption cross section of the object under study for left and right circularly polarized light,

$$\Delta\sigma = \sigma_L - \sigma_R, \tag{2.1}$$

where σ_L, σ_R represent the absorption cross sections for LCP and RCP, respectively. The dissymmetry factor g, defined as

$$g = 2\frac{\sigma_L - \sigma_R}{\sigma_L + \sigma_R}, \tag{2.2}$$

gives a measure of the differential circular absorption cross section normalized by the average absorption cross section. Equation 2.1 together with basic symmetry arguments shows that the mirror image of a chiral object presents the same absolute CD signal with the opposite sign. CD measurement as a function of light wavelength gives rise to a CD spectrum. Note that, even though the cross sections for right and left circularly polarized light may be large, the difference is generally very small for molecules, i.e., typically $g \leq 10^{-3}$ [5]. Therefore, CD studies on molecules are carried out by measuring the signal from a large number of molecules in ensemble-averaged experiments [9]. Because of the broad applicability of CD spectroscopy in biochemistry, it is highly desirable to improve its sensitivity, so as to analyse much smaller numbers of molecules, thereby reducing the amounts needed for chirality studies of newly synthesized compounds or for monitoring the conformational states of proteins.

To the chemist, chirality is a property of 3D objects which survives averaging over the random orientations of a macroscopic solution, as happens for chiral molecules. In microscopy or nanophotonics, however, we often deal with surfaces and nanostructures [10, 11] written by nano-lithography. Although they may be chiral in 2D (i.e., such a structure does not coincide with its 2D image in a reflection with respect to a line in its plane), they are not necessarily chiral in 3D because, at least in first approximation, they obviously present reflection symmetry in their own plane. In this case, dissymmetry in absorption of LCP and RCP light can arise from many different sources. The sample material itself can be chiral, either because of its structure, or because of defects induced by the fabrication process. The 2D-chiral shape of the structures, while not a source of 3D-chirality by itself, can combine

with front-back asymmetry to produce 3D-chirality. As discussed by Arteaga et al. [12], mirror symmetry of a 2D-chiral structure can be broken by the different refractive indices on either side of the interface, by inevitable surface roughness in sputtered or evaporated structures, or by the illumination process itself, as incident light usually comes from only one side of the sample. We use the term circular dichroism in this work, irrespective of the origin of the observed dissymmetry. Here, we present our experimental approach to image circular dichroism of single nanostructures, based on the differential detection of absorption by the photothermal effect rather than by the conventional extinction method, thus obtaining a photothermal circular dichroism (PT CD) image. Therefore, the plasmonic nanostructures in the present work are models of CD-active objects and are not used to enhance optical chirality signals, as proposed and realized by other groups [13, 14]. A similar approach, based on thermal lens spectroscopy, was used on solutions by Kitamori's group [15], and very recently has been proposed theoretically for the study of chiral nanoparticles [16]. The photothermal version of circular dichroism achieves an improved sensitivity in the detection of individual chiral nanostructures, as shown below, while relaxing experimental requirements needed for polarization control on the experimental setup.

2.2. Method

Figure 2.1 shows a conceptual scheme of the technique. For clarity we show the scheme for normal photothermal microscopy on the left-hand side and for PT CD on the right-hand side. We illuminate the sample with a heating beam (represented in green/dark green in the figure) that is absorbed by the nano-object under study, for example, a (2D) chiral plasmonic nanostructure, here represented as a left hand. We periodically modulate the polarization state of this heating beam between LCP and RCP at a frequency f_m (figure 2.1 (b)). As the chiral object presents different absorption cross sections for each handedness, the amount of absorbed energy differs for LCP and RCP light. The absorbed energy released as heat through non-radiative channels will thus increase the temperature of the nanostructure and create a non-uniform temperature distribution in the surrounding medium that will have slightly different amplitudes for LCP and RCP, as illustrated in figure 2.1 (b,f). This local temperature increase creates a time- and space-dependent change in the refractive index $\Delta n(\vec{r}, t)$ through the thermorefractive coefficient $\partial n/\partial T$ [17–19] of the surrounding medium [1], which is often called a thermal lens [20]. A second beam, the probe (represented in red in figure 2.1 (a) and (b)), is used to detect the strength of the thermal lens through interference between the reflection at the substrate-medium interface and the light back-scattered by the thermal lens [18]. The small difference in back-scattered light is detected by a lock-in amplifier at the polarization modulation frequency f_m. As the only difference upon modulation is the circular polarization state, the amplified signal will be proportional to the difference between LCP and RCP absorption, which is exactly the circular dichroism signal we seek. Non-chiral particles, having no difference in circular absorption cross sections, will not give rise to any PT CD signal.

Photothermal circular dichroism builds on the well established photothermal microscopy

[1] In the case of large metallic nanostructures, the temperature increase can modify the structure's optical response, for example by shifting its plasmon resonance. Therefore, large structures themselves can significantly contribute to the photothermal signal.

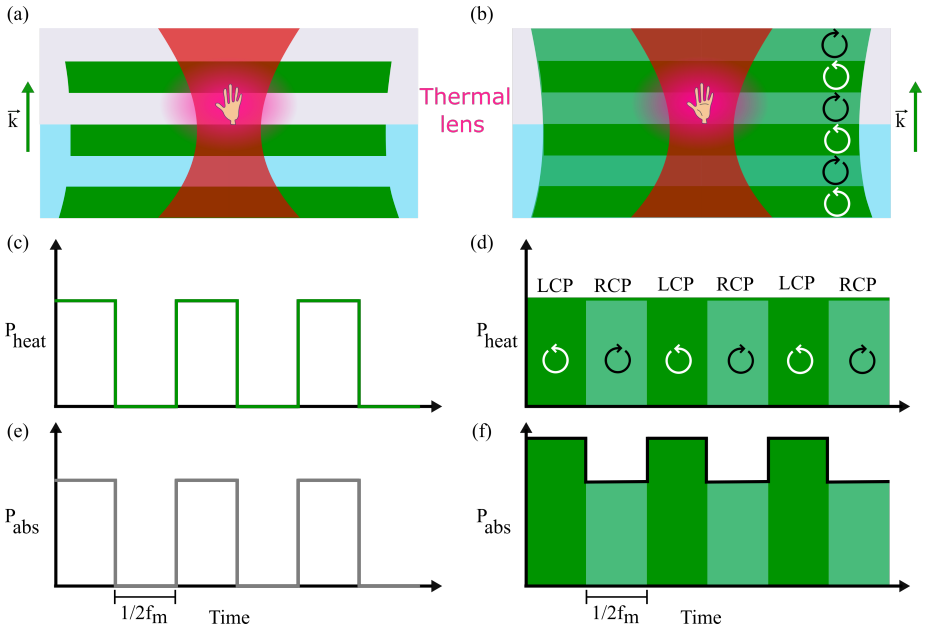

Figure 2.1: **Photothermal and photothermal circular dichroism concept**. (a) Scheme of the wide-field-heating photothermal detection of a chiral structure (illustrated as a hand) on a glass substrate. The heating beam is wide (green) and the probe beam (red) is focused to the diffraction limit. The heating beam intensity is modulated between on and off states at a frequency f_m. Part of the absorbed power will be released as heat to the environment, creating a thermal lens (in purple) around the absorbing object. The wavevector direction ($\vec{k}$) for both beams is shown. (b) Scheme for photothermal circular dichroism (PT CD), where we modulate the polarization state of the heating beam between left and right circularly polarized light (dark and light green, respectively). The thermal lens is also created in this case (in purple). The wavevector direction ($\vec{k}$) for both beams is shown on the right. (c) Time evolution of the heating power for the intensity-modulated photothermal microscopy, following the intensity modulation pattern at f_m. (d) Time evolution of the heating power for the polarization-modulated photothermal microscopy. In this case the heating power is *constant* and the only change is the polarization state. (e) Time evolution of the absorbed power by the nanostructure under study for the intensity-modulated photothermal case. Naturally, when the heating power is zero, the absorbed power is null. (f) Time evolution of the absorbed power by the nanostructure under study for the polarization-modulated photothermal case. Since it is a chiral structure, the absorbed powers for LCP and RCP are different.

to detect absorbing nanoscale objects such as plasmonic nanoparticles [17, 20–22], single conjugated polymer molecules [23] and even single small absorbing molecules at room temperature [24], and combines it with the enantioselective signal provided by circular dichroism.

Experimental setup. Sensing circular dichroism requires precise control of the polarization state. For that reason, great care must be taken with the illumination scheme and the choice of optical components. We implemented the concept of photothermal circular dichroism on a home-made optical microscope using a wide-field heating beam at a wavelength of $532\,\mathrm{nm}$ and a tightly focused probe beam at $780\,\mathrm{nm}$. In this way, we still obtain diffraction-limited spatial resolution through the tightly focused probe beam, whereas the polarization of the heating beam is easily controlled thanks to its low numerical aperture

($NA \sim 0.025$, corresponding to a spot diameter of $10\,\mu\mathrm{m}$).

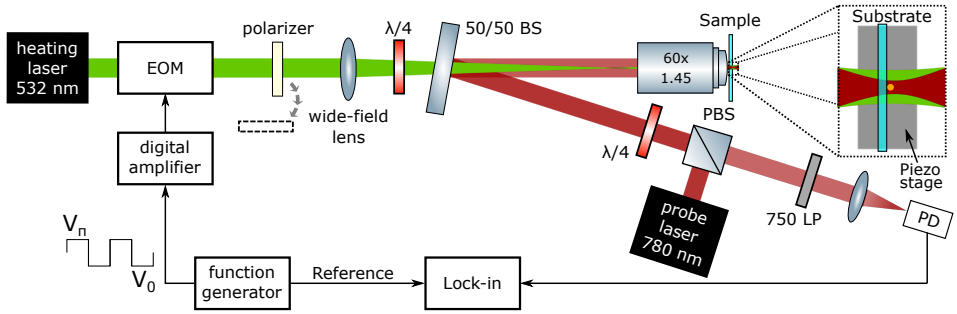

Figure 2.2: **Photothermal circular dichroism setup**. Implementation of the PT CD microscope using a $532\,\mathrm{nm}$-wide-field heating beam and a tightly focused probe beam at $780\,\mathrm{nm}$. The polarization modulation is achieved using an electro-optical modulator (EOM), leading to an alternatingly vertical and horizontal linear polarization state (the EOM acts as a zero and half-wave plate at 45 degrees with respect to the incoming polarization). A quarter-wave plate ($\lambda/4$) transforms these states into LCP and RCP light. The removable polarizer is added to achieve intensity modulation, i.e. conventional photothermal imaging. The wide-field lens focuses the heating beam in the back-focal plane of the objective to obtain wide-field illumination of the sample. The probe beam from a Ti:Sapphire laser is combined with the heating beam using a 50/50 beam splitter tilted by a small angle ($5°$). The detector (PD) is a fast photodiode with variable amplification. A long-pass filter (750LP) prevents direct detection of the heating beam. The generated signal is filtered by the lock-in amplifier set to the modulation frequency f_m created in the function generator and amplified to feed the EOM.

Figure 2.2 depicts a schematic representation of the microscope. The wide-field heating ensures a high-quality circular polarization state reaching the sample. This configuration is also less sensitive to possible lateral shifts in the heating beam due to mechanical drifts, thus improving stability. The heating and probe beams are combined via a non-polarizing beam splitter that is placed at a small angle (about $5°$) with respect to the heating beam to minimize the incidence angle's effect on the polarization state of the heating beam. We implemented a backward-detection for photothermal imaging, where the backscattered probe beam is sent to a fast photodetector (PD), and we suppressed noise efficiently with a lock-in amplifier. We used the an optical configuration, consisting of a polarization beam splitter and a quarter-wave plate to maximize the collection of photons scattered at the thermal lens [19]. We want to emphasize here that, despite the wide-field illumination of the heating beam, this technique is still confocal since the probe beam is focused tightly on the sample. To obtain an image, we scan the sample with a translation stage while the overlap of the two beams remains constant.

To implement photothermal circular dichroism, we need to modulate the heating beam's polarization between RCP and LCP. To this end, we use an electro-optical modulator (EOM) to rotate the incoming linear horizontal polarization by 90 degrees, at frequencies $\sim 100\,\mathrm{kHz}$. We set the EOM principal axis at 45 degrees with respect to the horizontal and we apply a square modulation of the EOM voltage between the zero-wave plate (V_0) and half-waveplate (V_π) values. Thus, after the EOM we have an alternating vertical (V) - horizontal (H) polarization state. Down the beam path, we use a quarter-wave plate with its axis at 45 degrees to transform these two orthogonal linear states into LCP and RCP, respectively. Additionally, we can add a linear polarizer directly after the EOM to perform conventional, intensity-

modulated photothermal imaging. More details about the experimental setup can be found in the Supporting Information of this chapter.

2.3. Results and discussion

As a model system for photothermal circular dichroism on single particles we prepared a sample containing 2D nano-structures of either handedness, presenting circular dichroism resonances in the visible range. The sample consists of an array of 2D-chiral gold nanostructures on a glass substrate in the form of gammadions, which present a strong chiral response in the visible due to the presence of plasmonic resonances [25, 26]. These structures are convenient to test circular dichroism measurements because their fourfold symmetry (C_4) implies that the linear dichroism ideally vanishes, provided the axis of rotational symmetry is oriented along the optical axis (as is the case presented here). Additionally, they can be easily fabricated in (2D) right- and left-handed versions. Note again that the design is based on the two-dimensional chiral character of the gammadions and that several effects can contribute to the circular dichroism signal, as discussed above [12, 27]. As an extra check, we also fabricated achiral structures with a similar shape.

Figure 2.3: **Handedness of gammadions**. Definition of the L- and R-handed structures based on their geometrical shape. The structures are supported by a glass substrate. We also show the coordinate system used for clarity.

We name our structures based on the geometrical properties: we call a gammadion "right-handed" if its arms point clockwise and "left-handed" if they point counter-clockwise, when we look at them from the top, which is defined such that the structures sit on top of the glass substrate. In figure 2.3 we show a scheme of the structures on the glass substrate, seen from the air side (above). This is a perspective view from the same side as used for the SEM images (see figure 2.4 (a) and (b)), but note that in the optical measurements we illuminate the structures from the bottom (from the glass substrate). For the wavelengths and structures used in this experiment, the left-handed enantiomer leads to a positive CD signal, as shown in figure 2.1[2].

[2]It is also important to note the convention used to define our polarization state. We follow the convention used

We fabricated an array of alternating right-handed, achiral and left-handed structures, as shown in the scanning electron microscopy images in figure 2.4 (a) and (b). In the Supporting Information we provide more details about the geometrical design of each type of structure and their locations in the array. With this array, we can measure the three types of structures in the same optical image and thus in the same experimental conditions. We embedded the structures in toluene to have a strong photothermal response (thanks to the high thermorefractive coefficient of toluene).

Figures 2.4 (c), (d) show conventional photothermal images of the whole array of structures under intensity modulation of the heating beam (c) and a higher-resolution image of the bottom right part of the array, (d). The intensity in these images is normalized to both the heating and pump intensities, deduced from powers and beam areas (A_h $78\,\mu\mathrm{m}^2$ and A_p $\sim 0.196\,\mu\mathrm{m}^2$, respectively), to allow for comparison of images recorded under different conditions. Photothermal images taken with circularly polarized light show different intensities from different structures due to the two different absorption cross sections of the three type of structures, chiral (right- or left-handed) or achiral, at the heating wavelength $532\,\mathrm{nm}$. Figures 2.4 (e) and (f) depict the photothermal circular dichroism images of the same areas as (c) and (d), where we clearly observe contrast for the right- and left-handed structures, with opposite signs, and hardly any signal from the achiral structures, demonstrating the desired enantioselectivity of the technique. We note that the signal-to-noise ratio (SNR) for the PT CD images is excellent, in the order of 40 with only $30\,\mathrm{ms}$ integration time in the lock-in amplifier and with moderate intensities used for imaging. For example, when we take the signal of the top left structure of figure 2.4 (f) and we average the pixels corresponding to the size of the point-spread function we obtain a signal $S_{stru} = -(1.53 \pm 0.01)10^{-2}\ \mathrm{mV\,mW^{-2}}$, while the standard deviation with the same number of pixels outside any structure gives $N = (3.8 \pm 0.1)10^{-4}\ \mathrm{mV\,mW^{-2}}$, so the signal-to-noise ratio for this specific structure is $S_{stru}/N = SNR \sim 45$. We note that the value for the noise mentioned above is similar to the value we measured when we turned off the heating laser and performed an image only with the probe laser. This is a significant improvement in sensitivity for detecting circular dichroism of individual chiral nanostructures with respect to the extinction-based detection schemes, in which a $SNR \sim 10$ is typically obtained when using a $1\,\mathrm{s}$ integration time on the resonance of similar gold nanostructures [26].

It is important to note that the imaging conditions for this sample are not optimized. First, the heating beam at $532\,\mathrm{nm}$ is not in resonance with the strongest CD resonance of the structure in the visible range, located at $\sim 700\,\mathrm{nm}$ according to our numerical simulations. Second, due to the non-negligible absorption at that wavelength, the probe laser intensity at $780\,\mathrm{nm}$ had to be kept low ($I_p = 0.76$ mW/$\mu\mathrm{m}^2$) to avoid boiling the surrounding liquid, and reshaping of the structures at still higher powers. For the numerically calculated absorption spectra and g-factor, please refer to the Supporting Information. The photothermal circular dichroism images in figure 2.4 (e) and (f) are proportional to the numerator of the dissymmetry factor g (defined in equation 2.2), while the photothermal images (c) and (d) are proportional to σ_L, since we used an intensity-modulated heating beam with left circular polarization to take those photothermal images. Thus, we can use the signals from

by Jackson [28], where an observer facing the incoming plane wave with left circularly polarized state sees a counter-clockwise rotation. This corresponds to the tip of the electric field vector tracing out a left-handed helix (positive helicity).

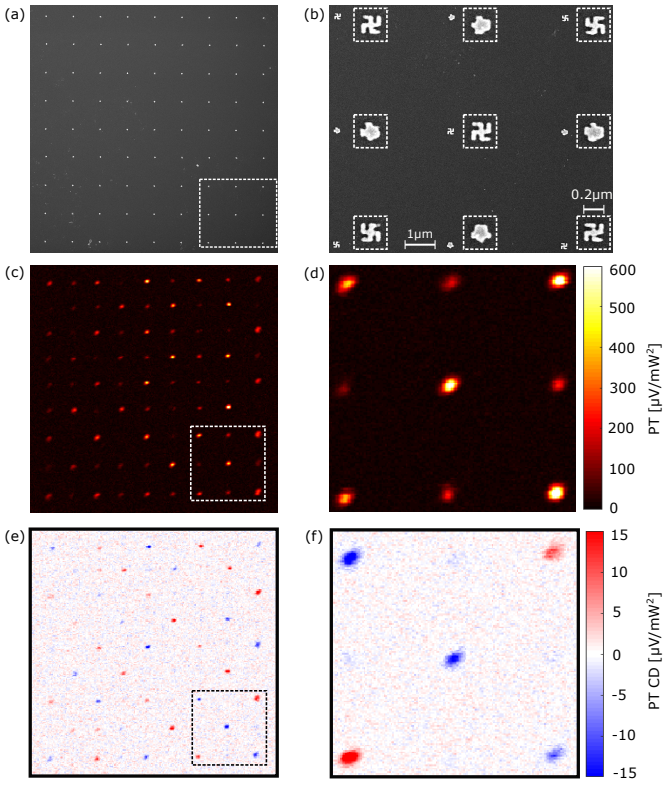

Figure 2.4: **Chirality-sensitive photothermal imaging**. (a) Scanning electron microscope (SEM) image of a 9×9 nano-gammadions array. From the 81 nanostructures, 20 are left-handed, 21 right-handed and 40 achiral. The distance between the individual nanostructures is $4\,\mu m$ in both directions. (b) Higher resolution SEM image of the bottom right part of the array (the dashed rectangle in (a) shows the area for this image). Detailed images of the structures are shown in the dashed boxes, right of each structure. The scale bars are to show the average distance between two gammadions and the average size of the individual gammadions. (c) Photothermal (PT) image of the complete array, displaying the signal of each structure. We normalized the image with the heating power ($P_h \sim 9\,mW$) and the probe power ($P_{probe} \sim 150\,\mu W$). (d) Higher resolution photothermal image of the area shown in (b). (e), (f) Photothermal circular dichroism (PT CD) images of the areas in (a) and (b), respectively. We also normalized the images using the heating and probe powers. These images show a clear change of sign in the signal, following the chirality of the nanostructures. As expected, the nominally achiral structures show nearly zero signal. Note that the optical and SEM images cannot be overlapped because they are observed from different sides of the interface.

these images to calculate g for every structure fabricated. For this, we averaged the signal from 3×3 pixels centred at the maximum signal of each bright spot on figure 2.4 (c) and (e). Since we have correlated optical and geometrical information of our structures, we can distinguish structures with the same handedness: right-handed, left-handed and achiral (the top right, top left and top centre structure in figure 2.4 (b), respectively), and analyze their PT CD signals.

Figure 2.5 (a) shows the results for the g-factor of the 81 structures in the array correlated with their respective photothermal signals, using different colors and symbols for the three

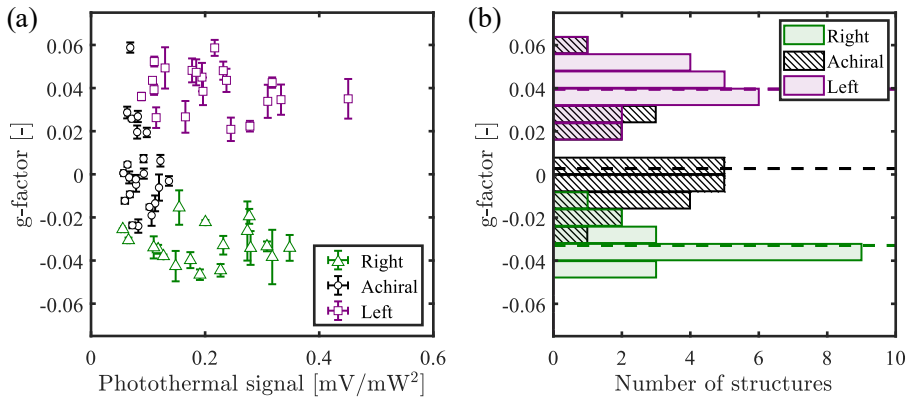

Figure 2.5: **Chirality-sensitive signal analysis.** (a) Dissymmetry factor g vs. photothermal signal for the 81 nanostructures, separated by groups according to the handedness. The inserts show the corresponding handedness for each group. We observe that the data for each group are clustered together and present some dispersion, presumably due to fabrication imperfections. (b) Histograms of g-factors for the three types of structures. We can clearly see different distributions, showing our ability to distinguish chiral and non-chiral structures. The mean g-factor for each group of nanostructures is shown in the figure as dashed horizontal lines. We assign the width of these distributions mainly to fabrication imperfections.

groups. We observe a clear separation of these groups according to their signals: we obtain positive values for left-handed structures (violet squares), negative values for the right-handed structures (green triangles) and values close to zero for most achiral structures (black dots). Every structure may have its particular fabrication imperfections which give rise to the observed distribution of g-factors, in addition to, but without clear correlation with, the size and shape variations responsible for the dispersion in photothermal signals. The histograms for g-factors are shown on figure 2.5 (b). The mean values of these distributions correspond to $g_L = (3.9 \pm 0.2) \times 10^{-2}$, $g_a = (3 \pm 3) \times 10^{-3}$ and $g_R = -(3.3 \pm 0.2) \times 10^{-2}$ for left, right and achiral structures, respectively. Despite the fabrication fluctuations, the obtained mean values for the distributions are as expected from the handedness of the structures. Moreover, they are in agreement within a factor of 2 with the values obtained using numerical simulations for the ideal gammadions, which give $g_L \sim 0.061$ at $532\,\mathrm{nm}$ for the left-handed structure. The Supporting Information (section 2.5) provides the full spectra and more details on the numerical simulations. The difference between simulated and measured data may be attributed to fabrication imperfections of the structures. In addition to measuring circular dichroism, we can easily modify our experimental setup to measure linear dichroism (LD) in any desired frame of two orthogonal axes. It suffices to exchange the quarter-wave plate for a half-wave plate to rotate the vertical and horizontal polarization states after the electro-optical modulator to the desired axis. We call this photothermal linear dichroism (PT LD). It is well known that LD is usually much stronger than CD. We thus performed a set of LD measurements on the same gammadions shown in figure 2.4 (b) in two different directions: $0, 90$ degrees (modulation V-H, i.e. without any waveplate after the EOM) and $45, 135$ degrees. Although both signals should vanish for perfect gammadions, we observed non-zero LD. We attribute this LD to the imperfections in the nanofabrication.

For the detailed experimental results, refer to the Supporting Information.

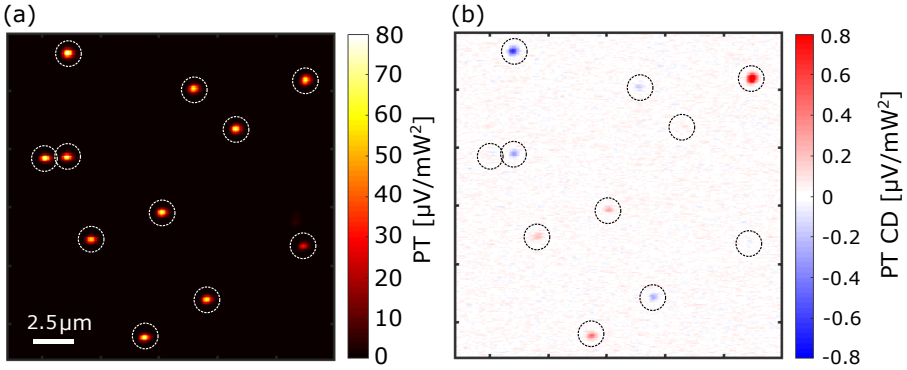

Figure 2.6: **Circular dichroism of individual nanospheres.** (a) Photothermal (PT) image showing several gold nanoparticles, diameter 100 nm, on glass. Note the high uniformity of the spots in shape and intensity. (b) Photothermal circular dichroism (PT CD) image of the area shown in (a). Although most particles show low chirality signals, two particles have high negative (upper left corner) or positive (upper right corner) chiral signals. The g values for them are -0.83% and 1.82%, respectively. Dashed circles are guides to the eye.

As a next step, we prepared a sample with gold nanospheres of 100 nm diameter dispersed on a glass substrate and again we immersed this sample in toluene. Figure 2.6 (a) shows a photothermal image and (b) the corresponding photothermal circular dichroism image. In this case, as the plasmonic resonance of the spheres is around 550 nm, the imaging conditions are close to optimal: we used a high intensity of the heating beam (heating power P_H =16 mW) that is efficiently absorbed, and at the same time we increased the probe intensity to $I_p = 5000$ kW/cm^2. Because of the low absorption of the nanospheres at 780 nm, this larger probe intensity did not lead to significant heating. The calculated temperature increase at the probe power is 16 K. Therefore, we were more sensitive to chirality in these experimental conditions than in the experiments on gammadions.

We observe that many particles show a dim signal, close to zero, as expected for achiral structures such as spheres. However, some particles show a strong signal, either positive or negative (see two examples in Fig. 2.6 (b)). We also performed High-Angle Annular Dark-Field Scanning Transmission Electron Microscope (HAADF-STEM) imaging of gold nanospheres to obtain information about morphology and the crystalline structure of the particles. We found that some particles show defects in their crystalline structure and are non-spherical in shape (see Supporting Information for the images and more details). We therefore assign the chirality signals to the non-spherical shape and defects of nanospheres. We cannot assign the strong chirality signals to residual aggregates of nanospheres, as the photothermal signals of all particles are very uniform, indicating single nanospheres of very similar dimensions and ruling out dimers or higher aggregates. A correlation plot of photothermal signals and g-factors and the histograms of photothermal signals and g-factors for many single gold nanospheres are shown in the Supporting Information (figure S2.9).

To further test the influence of linear dichroism in the sample on our PT CD signal, we measure both PT CD and PT LD on the sample of gold nanospheres. We observed a LD signal approximately 10 times bigger than the CD signal with no clear correlation showing

that the cross talk of LD into our signal is smaller than 10%. More details about this set of measurements can be found in the Supporting Information.

2.4. Conclusion

In summary, we presented an optical method, photothermal circular dichroism, that enables us to measure the chirality of absorbing nanostructures with unprecedented signal-to-noise ratio. We experimentally showed the enantioselective character of the signal by imaging right- and left-handed plasmonic structures with quantifying dissymmetry factors $g \sim 0.04$, measured with a signal-to-noise ratio of up to 40. From estimated errors in the factors measured, we believe we could measure dissymmetry factors as small as $g_{min} = 0.004$, which approaches the orders of magnitude needed to study biological molecules in small quantities.

Photothermal circular dichroism extends the capabilities of circular dichroism due to the increased sensitivity, extending the applications of the technique to smaller quantities of analytes or shorter experiment times. Our results demonstrate several advantages of photothermal circular dichroism. First, as our detection scheme relies on measuring the local temperature increase of the nanostructure under study due to the absorption of heating photons of a controlled polarization, the polarization state of the probe light scattered by the thermal lens is irrelevant. We only need to control the polarization state of the heating beam carefully. This is in contrast to the extinction [26] or scattering-based [29, 30] detection of circular dichroism, where the polarization state of the complete beam path has to be carefully controlled. Second, since we are imaging with a photothermal-based technique, our signal can be optimized as reported earlier for photothermal signals [19]. With available tunable laser sources for the heating beam, photothermal circular dichroism can also be extended to circular dichroism spectroscopy.

2.5. Supplementary information

2.5.1. Details of the experimental setup

The schematic of our photothermal circular dichroism setup is shown in figure 2.2. Here, we explain all the components in detail. We used a Coherent Verdi laser (Model: V10-A0366, wavelength of $532\,\mathrm{nm}$) as a heating beam which was passed through an electro-optical modulator (EOM) from Qioptiq (Model: LM0202) for modulating between two orthogonal linear polarizations. The modulation frequency was set by a function generator (from Tektronix, Model: AFG3102) which sends the signals to a digital amplifier (from Qioptiq, Model: DIV20) to amplify the signal before sending it to the EOM. The function generator sends the same signal also to the lock-in amplifier (from Stanford Research Systems, Model: SR844) as a reference signal. For Koehler-like illumination a lens with focal length of $50\,\mathrm{cm}$ was used to focus the heating beam at the back focal plane of an oil-immersion objective (from Olympus, PLAPON, 60X, NA = 1.45) and to illuminate the back focal plane of the objective with low numerical aperture (NA ≈ 0.025 which corresponds to a diffraction-limited spot of $10\,\mu\mathrm{m}$ diameter). A quarter-wave plate (Thorlabs) was used to convert the linear polarization to circular and thus, we modulated the heating beam between left and right circular polarization to measure photothermal circular dichroism. The polarization state of light was analysed using a polarization analyser (Schaeffter and Kirchhoff SK010PA-VIS).

A non-polarizing $50/50$ beam splitter (Thorlabs) was used to transmit the heating beam and to reflect the probe beam. The collimated probe beam (Ti-Sapphire laser from Spectra-Physics, wavelength $780\,\mathrm{nm}$, Model: 3900S) was focused by the objective in the focal plane. To detect the back-scattered probe beam signal efficiently, we used a combination of polarizing beam splitter (PBS) and quarter-wave plate. The back-scattered probe signal was then filtered out from the heating beam by using a long-pass (750 LP) filter and focused into a photodiode (PD) from Femto (Model: DHPCA-100-F, with an amplification of 10^6) using a lens of focal length $7.5\,\mathrm{cm}$. We note that the reported laser powers are measured just before the oil-immersion objective. The photodiode signal was then sent to the lock-in amplifier as an input signal. A flippable polarizer was used to switch between normal photothermal and photothermal circular dichroism measurements. For normal photothermal microscopy, we inserted a polarizer after the EOM to achieve intensity modulation and for the photothermal circular dichroism, we removed the polarizer to keep the modulation between left and right circular polarizations. To obtain an image, we scan the sample by translating the sample stage using a piezo stage (PI P.611.3.5 Nanocube) while keeping the overlap between the heating and probe beams constant.

2.5.2. Sample design and preparation

We designed a sample that contains an array of alternating structures following the pattern showed in figure S2.1 (left). We have three types of structures: left (L), right (R) and achiral (A). The individual designs and dimensions of these structures are shown in figure S2.1 (right); all the structures have a height of $70\,\mathrm{nm}$.

The sample with the array of nanostructures was prepared using e-beam lithography and

lift-off. First, glass coverslides were cleaned by sonication in acetone and then in isopropanol for 5 minutes. Next, the coverslides were coated with PMMA e-beam resist in the following steps: 1) Dehydration of the glass slide surface by baking on a hot plate at 180 °C for 5 minutes, 2) Spin coating PMMA 950K, dilution 6% in anisole at 4000 rpm, which results in 300 nm layer thickness, 3) Baking the glass slide for 5 min at 180 °C. After spin-coating, the samples were coated with 15 nm of Cr using Temescal FC-2000 e-beam evaporator. This sacrificial layer of Cr serves to prevent charging effects on glass during e-beam patterning. The pattern was written using e-beam (Raith EBPG 5000+) with a beam step size of 1 nm and a dose of 2000 $\mu C/cm^2$, which was found to be optimal through a dose test. Following the exposure, the Cr layer was stripped by wet etch in TechniEtch Cr01 (MicroChem) for 25 s and the sample was rinsed with deionized water. The pattern was developed by submerging the sample for 1 minute in a mixture of MIBK (methylisobutylketone) and IPA (isopropanol) (1:3 v/v) and further submerging into IPA for 1 minute. Finally, 70 nm of gold was evaporated onto the sample using a Temescal FC-2000 and followed by a lift-off procedure (10 minutes in n-methylpyrrolidone at 80 °C). The sample was then rinsed with acetone and IPA and spin-dried at 2000 rpm. After nanofabrication we prepared the sample for the optical measurements. We sandwiched the sample with a second cavity glass slide (Menzel number 1.5) to provide space for a liquid. We chose toluene as a liquid medium because it provides a high thermorefractive coefficient ($\partial n/\partial T = -5.68 \times 10^{-4}$ K^{-1}) which is essential for PT imaging [19]. After optical imaging, the sample was sputtered with 5 nm of platinum to make it conductive for proper imaging under a scanning electron microscope (SEM). SEM images are shown in figure S2.4

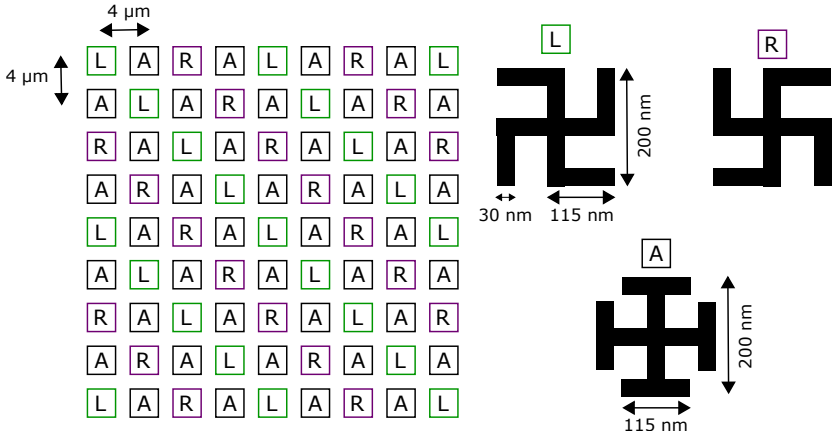

Figure 2.1: **Design of the checkerboard sample**. (Left) Array design, showing the alternation of the three types of structure: left (L), right (R) and achiral (A). (Right) Detail of the design of each type of structure. The height of the structures is 70 nm.

2.5.3. Numerical simulations

We performed numerical simulations to calculate the absorbed power for right and left circularly polarized light by the idealized gammadions structures on a glass substrate embedded in toluene. The dimensions used for the simulations are the ones depicted in figure S2.1 on the right, with a height of 70 nm. We used the commercial FDTD software Lumerical with a total-field scattered-field source [31] to simulate the plane wave heating laser and we calculated the absorbed power by the structures as

$$P_{abs} = -\frac{1}{2}\omega|\mathbf{E}|^2\Im(\epsilon)\,, \tag{2.3}$$

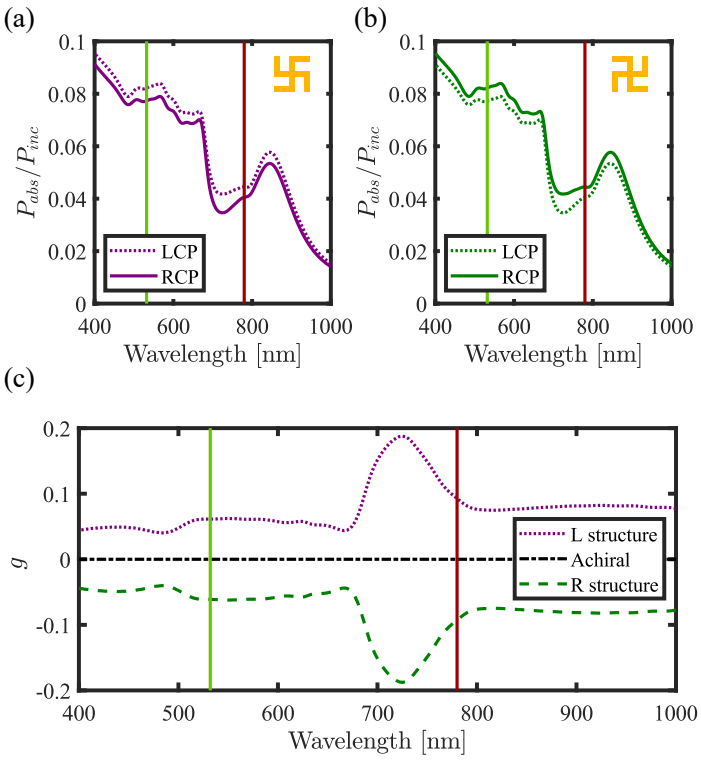

Figure S2.2: **Absorption and g-factor numerical results for ideal gammadions**. (a) Normalized absorbed power for a single left-handed gammadion structure (shown in the inset) on a glass substrate embedded in toluene. Note that the structure is now seen from the glass side and corresponds to the definition of figure 2.3 as left-handed. The absorption for LCP is higher than for RCP. (b) Normalized absorbed power for the right-handed gammadion structure (shown in the inset) on a glass substrate embedded in toluene. For this right-handed structure, the absorption for RCP is higher than for LCP. (c) Dissymmetry factor g as defined in equation 2.2 for both structures. Additionally we show the achiral structure, showing null chirality, as expected from symmetry arguments. The vertical lines in the plots correspond to the heating wavelength, 532 nm (in green), and the probe wavelength, 780 nm (in red). The absolute value of g at the heating wavelength is ~ 0.061.

where ω is the frequency of the incoming wave, $\mathbf{E}$ is the electric field in the structure and $\Im(\epsilon)$ represents the imaginary part of the permittivity [32]. Note that this is calculated for every voxel in the simulation and then integrated over a $800\,\mathrm{nm}\times800\,\mathrm{nm}\times800\,\mathrm{nm}$ volume to calculate the total absorbed power for each illumination conditions. We also calculated the absorption cross section of the gammadions at $532\,\mathrm{nm}$, obtaining $2.2\times10^4\ \mathrm{nm}^2$. In the simulation, we place the R or L gammadions made of gold on a glass substrate. For the gold structure we took the dielectric function built in the software (Gold (Au) - CRC) [33] and the one of glass from Palik [34]. The refractive index of toluene was taken from the work by Kedenburg et al. [35].

We excite the structure with a plane wave coming from the substrate side, using left and right circularly polarized light (equivalently to what we do experimentally) and for each case we calculate the absorbed power normalized by the incident power P_{abs}/P_{inc}. Figure S2.2 (a) shows the obtained spectra for both circular polarizations states for the left-handed structure and figure S2.2 (b) for the right-handed structure. Note that the former absorbs more when excited with LCP and the opposite situation holds for the latter. The vertical lines show the locations of the heating beam (green) and the probe beam (red), for reference.

Figure S2.2 (c) shows the dissymmetry factor spectra $g(\lambda)$ for both structures. Naturally, they only differ in the sign, being positive for the L structure and negative for the R structure in the studied range. For completeness we also simulated the achiral ideal structures, that exhibit null dissymmetry factor. Note that the calculated value for the dissymetry at the heating wavelength is $g\sim0.061$. We also checked that the g-factor values flip sign when we repeat the simulation with an exciting wave coming from the solvent side (we changed the wavevector from $\vec{k}\propto+\hat{z}$ to $\vec{k}\propto-\hat{z}$). This is the expected behaviour since the gammadions seen from the opposite side will have the opposite handedness.

2.5.4. Measurement of linear dichroism on gammadions

Linear dichroism is defined as the differential absorption between two orthogonal linear polarizations states:

$$LD_{\hat{\vec{n}}}=\sigma_{\parallel}-\sigma_{\perp}, \tag{2.4}$$

where $\sigma_{\parallel}$ and $\sigma_{\perp}$ represent the absorption cross section for a polarization state parallel and perpendicular to a direction given by the vector $\hat{\vec{n}}$, respectively. We performed different measurements of photothermal LD in the horizontal direction, by modulating the incoming polarization state of the heating beam between linear horizontal and vertical polarization states. To achieve this we removed the quarter-wave plate from the setup. We also measured with respect to the diagonal state (rotated $45°$), obtained by adding a half-wave plate. The reason for doing these two types of polarization modulations is to obtain full information about the linear dichroism signals. Figure S2.3 shows the photothermal LD images of the same gammadion structures as shown in figure 2.4(b). We clearly see non-zero linear dichroism signals, of similar order but stronger than circular dichroism signals. We attribute this to the fabrication imperfections in the sample, which break the symmetry of the structures. As figure S2.3 (d) shows, there is no obvious correlation between LD and CD.

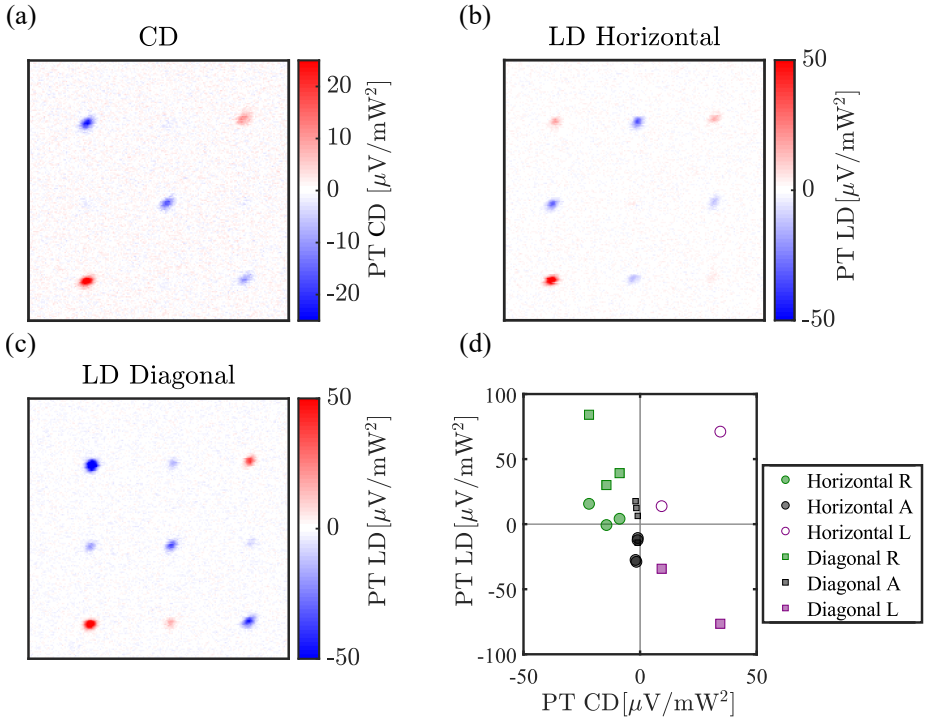

Figure S2.3: **Linear dichroism measurements of the gammadion sample**. (a) Photothermal circular dichroism image of 9 gammadions (the same as shown in figure 2.3 (b) and (d)). (b) Photothermal linear dichroism image of the same area as (a), with horizontal-vertical modulation (90° and 0°). (c) Photothermal linear dichroism in the diagonal direction, i.e. polarization modulation between 45° and −45°. (d) Correlation plot of the PT CD and PT LD.

2.5.5. Characterization of nanospheres shape and size

We studied in detail the morphological characteristics of the nanospheres used for the optical imaging by performing High-Angle Annular Dark-Field Scanning Transmission Electron Microscope (HAADF-STEM) imaging on a dispersion of such nanoparticles. The HAADF-STEM images were acquired using a Thermo Fisher Scientific Tecnai Osiris microscope operated at 200 kV with a 50 pA beam current and a frame time of 6 s. All tomography series were acquired by taking projection images over an angular range of ±75° with a tilt increment of 3° with a frame time of 6 s. After alignment of the projection images by using a cross correlation, the stacks of aligned projection images served as inputs for 20 iterations of the expectation maximization reconstruction implemented in the ASTRA toolbox [36]. Figure S2.4 shows representative HAADF-STEM images of gold nanospheres from the same synthesis batch at different resolutions. In figure S2.4 (a) we present a zoom on the remarkably non-spherical particles, marked with an arrow. In figure S2.4 (b) we zoom in further and again present in the rectangles a closer image of a few non-spherical particles. Figures S2.4 (c) and (d) depict higher resolution images where the facets of some of the nanoparticles im-

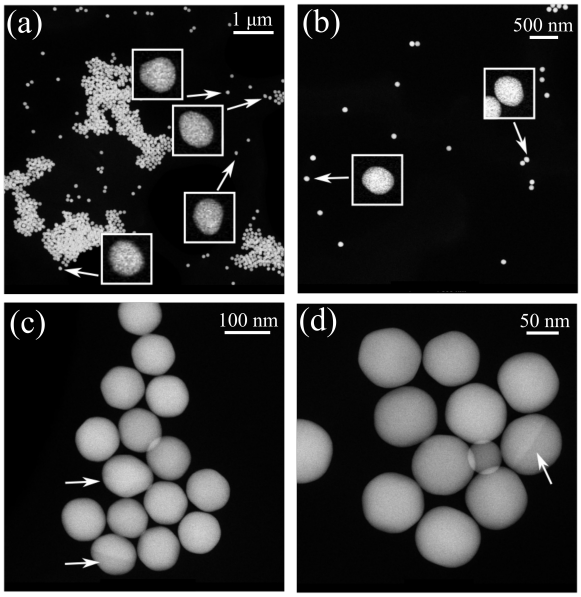

Figure S2.4: **HAADF-STEM images of gold nanospheres**. (a) Large area scan to provide an overview of many nanoparticles. The rectangles contain a zoomed image on the particles marked with arrows, where non-spherical shape is clearly observed. (b) Image of a different area of the sample, with higher magnification than in (a). Again, we show in the rectangles a zoom on the particles marked with arrows. (c) Higher resolution image of a cluster of nanoparticles. The arrows depict the particles with the strongest deviation from spherical shape. (d) Closer look on another cluster of particles, where the arrow now depicts a particle with defects in the crystalline structure. Most particles exhibit faceted spherical-like shapes. However, a fraction of the nanospheres are anisotropic and/or exhibit crystal defects as evident from the contrast difference. Examples of such particles are marked by arrows in the images. The scale bars are shown in each panel.

aged can be clearly appreciated. The arrows point to the non-spherical shaped nanoparticles we found. In addition, the arrow in figure S2.4 (d) shows a particle with defect in the crystalline structure. From the 2D images it can be observed that most nanospheres are isotropic. However, some nanospheres display lattice defects or are anisotropic. The defects are most likely twin boundaries as evident from the contrast difference in the HAADF-STEM images for such particles. Because the displayed images are only 2D projections of the real 3D object, we also performed electron tomography to obtain the 3D shape of a characteristic nanosphere. In addition, we quantified the size distribution of our sample of nanoparticles by extracting the measured the radius from STEM images. The obtained histogram is depicted in figure S2.5. While the nominal radius given by the manufacturer (Nanocomposix) is $100\,\mathrm{nm}$ we measured an average value of $94\,\mathrm{nm}$.

2.5.6. Does linear dichroism influence photothermal circular dichroism?

In order to characterize the crosstalk in our photothermal circular dichroism signal with linear dichroism, we measured both circular dichroism and linear dichroism of the same nanoparticles, characterized in the previous section. Figure S2.6 shows photothermal, pho-

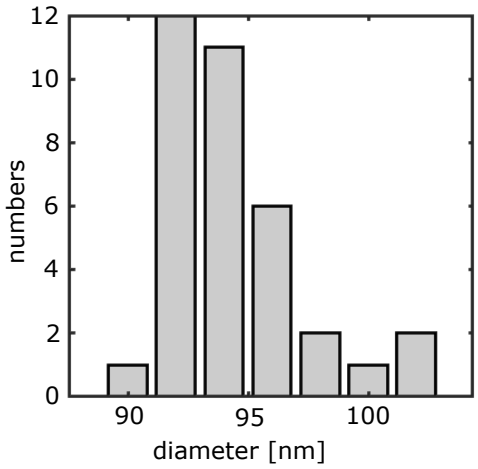

Figure S2.5: **Size distribution of the nanoparticles from HAADF-STEM**. The particle sizes are calculated from 35 single particles from the images shown in figure S2.4 (b). The average particle size is 94 nm with a size dispersion of 3%.

tothermal circular dichroism and photothermal linear dichroism signals of single 100 nm gold nanospheres. The value of the nanosphere size is 100 nm provided by the manufacturer, however the average particle size calculated from STEM image is rather 94 nm (see

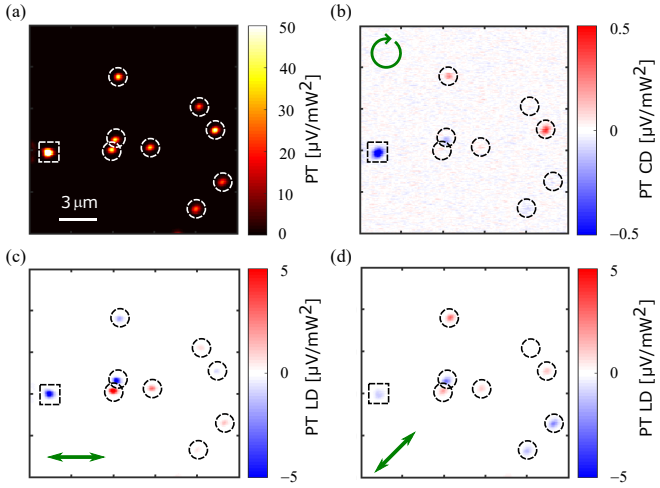

Figure S2.6: **Circular dichroism and linear dichroism measurements of gold nanospheres**. (a) Photothermal (PT), (b) photothermal circular dichroism (PT CD), (c) photothermal linear dichroism (PT LD) with 90° and 0° (horizontal-vertical) polarization modulation and (d) photothermal linear dichroism (PT LD) with −45° and 45° (diagonals) polarization modulation. Dashed circles are drawn to show single particle spots. The left-most particle is probably an aggregate and marked with a dashed square box. The arrows show the direction $\vec{n}$ for the LD.

figure S2.5). Note that the colour scale in photothermal circular dichroism and photothermal linear dichroism images are 100 times and 10 times smaller than PT image, respectively. Most particles show weak circular dichroism but strong linear dichroism signal. This indicates that there is little crosstalk between the photothermal circular dichroism signal and linear dichroism. We attribute the linear dichroism signal of nanospheres to shape and crystallinity imperfections of individual nanoparticles. All the images of PT CD and PT LD of gammadions and gold nanospheres are X channel signals of lock-in to show phase information. We chose X channel signal instead of Y channel because at our measurement modulation frequency, most nanostructures or nanoparticles show in-phase signals.

2.5.7. More measurements of circular dichroism of gold nanospheres

We measured photothermal (PT) and photothermal circular dichroism (PT CD) of single 100 nm gold nanospheres deposited on a glass substrate. The images for two different areas in both imaging modes are shown in figure S2.7. Most particles show weak photothermal circular dichroism signals and are distributed between positive and negative PT CD signals.

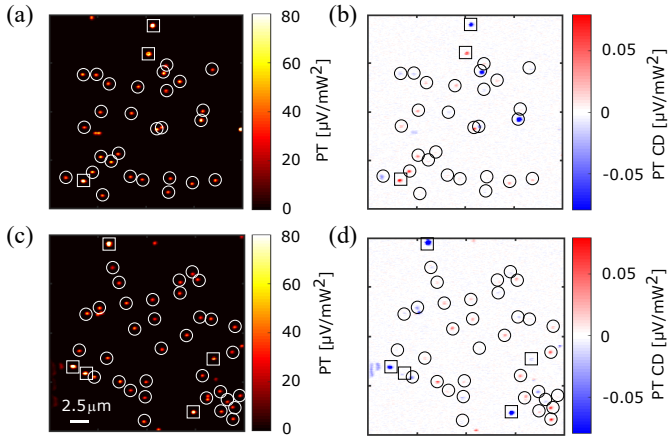

Figure S2.7: **Circular dichroism measurements of gold nanospheres on glass**. (a) Photothermal (PT) image of an area showing many nanospheres. Note the small dispersion in PT intensities, showing a remarkably small dispersion in size for the nanoparticles. (b) Photothermal circular dichroism (PT CD) of the same area as (a). (c) Photothermal (PT) image of a different area of the sample, showing more nanospheres. (d) Photothermal circular dichroism (PT CD) of the same area as (c). The solid circles are drawn to show correlative image spots between PT and PT CD images and to show which particles are considered for the correlation and histogram analyses. Extremely bright particles (marked with solid square boxes) in the photothermal image are probably aggregates and were ignored for the analysis. We also ignored the particles which are on the edge of the scan for the analysis.

We calculated the g-factor by averaging the signal of 3×3 pixels at the maximum intensity for each spot in the images, excluding exceptionally bright spots in both photothermal and photothermal circular dichroism images, which are assigned to clusters of nanoparticles. We used equation 2.2 for the g-factor definition. A correlation plot of g-factor and photothermal signal of 59 single gold nanospheres is shown in figure S2.8 along with corresponding histogram of g-factors. Most particles show g-factors less than 1% and normally distributed

between positive and negative signals, with a small mean value of 0.16% (which may be the experimental bias). For a perfect spherical particle, photothermal circular dichroism is

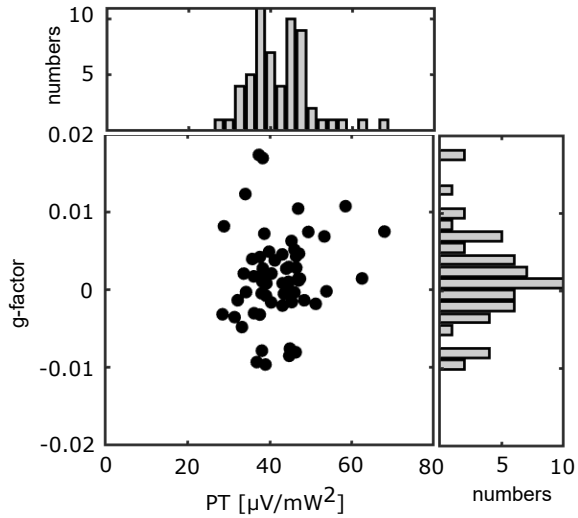

Figure S2.8: **Histogram of PT and PT CD of gold nanospheres on glass**. Correlation plot of measured g-factor and photothermal signal and histograms of photothermal signal and g-factor. The histogram of photothermal signal looks narrow, which is consistent with the histogram of particle sizes shown in figure S2.5. The dispersion in particle size is 3% and the dispersion in photothermal signal is 18%. The distribution of photothermal signals follows from the distribution of particle sizes, and from the dispersion in orientations and shapes of the nanoparticles (as we see in figure S2.4). Most particles show g-factors less than 1%. The mean value of g-factor is 0.0016.

expected to be null. However, a fraction of particles in our measurements are non-spherical in shape and have defects in their crystal structure as we see from the STEM images in figure S2.4. We therefore attribute the observed photothermal circular dichroism signal to the particle's shape and defects. To understand in detail how the particle shape and defects play role in the photothermal circular dichroism signal, a careful correlated optical and TEM-tomography should be performed, which is outside the scope of this work.

2.5.8. Line profiles of PT and PT CD signal of gold nanospheres

To further characterize our PT-CD microscope, we present here representative cross sections from our optical images when the object imaged is smaller than the diffraction limit, i.e. we show a linear profile of the point-spread-function (PSF) of our microscope. The line profiles of PT and PT CD signals of two gold nanospheres are shown in figure S2.9. The point-spread functions of both PT and PT CD signal look similar except for some wrinkles appearing as side bands in PT CD profile. These wrinkles are attributed to low signal-to-noise ratio in PT CD signal.

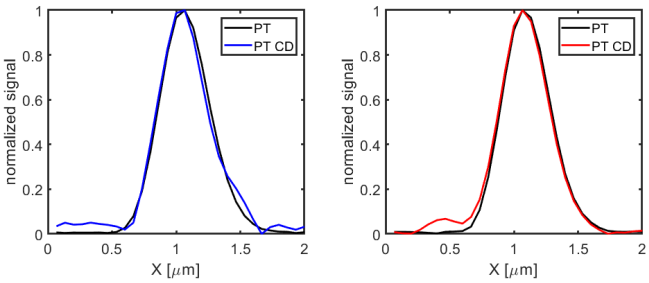

Figure S2.9: **Line profiles of PT and PT CD of gold nanospheres**. Line profiles of PT and PT CD signal of two gold nanospheres. (Left) the line profiles of the top left particle in figure 2.6 (a), (b) and (right) the line profiles of the top right particle in figure 2.6 (a), (b). Please note the color of the PT CD line profiles (same color as in figure 2.6 (b)). For the particle with negative PT CD signal, the line profile is shown with absolute values. All line profiles are normalized by the maximum peak signals.

2.5.9. Temperature increase due to absorption of the heating and probe beams

The (local) increase in temperature of a nanostructure due to light absorption in the steady state case for a sphere can be calculated as

$$\Delta T = \frac{P_{disp}}{4\pi\kappa R}\,, \tag{2.5}$$

where P_{disp} is the power dissipated by the nanosphere, κ is the average thermal conductivity of the medium and the glass substrate ($\kappa = (\kappa_{medium} + \kappa_{glass})/2$) and R is the radius of the nanosphere [37]. With our experimental parameters, we obtained ΔT_{sphere} of 8 K and 16 K at the heating and probe powers, respectively.

When the structure is not spherical in shape, as it is for our gammadions, there is no simple expression to calculate the temperature increase. However, a common approach for other nanostructure shapes is to use equation 2.5 replacing the radius R with a fictitious radius R_L that can be calculated for different geometries [37]. Thus, we used R_L =200 nm in this equation to approximate the increase in temperature, obtaining 11.7 K and 97.5 K at the heating and probe powers, respectively. The boiling temperature of toluene (393 K, or 120 °C, taking surface tension into account) provides an upper bound for the maximum temperature reached by the gammadion.

References

[1] Kelvin, W. T. B. *Baltimore lectures on molecular dynamics and the wave theory of light*; CJ Clay and Sons, 1904.

[2] Schäferling, M. *Chiral Nanophotonics*; Springer, 2017; p 159.

[3] Alberts, B.; Johnson, A.; Lewis, J.; Raff, M.; Roberts, K.; Walter, P. *Molecular biology of the cell*, 6th ed.; Garland Science: New York, 2010.

[4] Siegel, J. S. Biochemistry: Single-handed cooperation. *Nature* **2001**, *409*, 777.

[5] Fasman, G. D. *Circular dichroism and the conformational analysis of biomolecules*; Springer Science & Business Media, 2013.

[6] Beychok, S. Circular dichroism of biological macromolecules. *Science* **1966**, *154*, 1288–1299.

[7] Berova, N.; Nakanishi, K.; Woody, R. W. *Circular dichroism: principles and applications*; John Wiley & Sons, 2000.

[8] Johnson Jr, W. C. Secondary structure of proteins through circular dichroism spectroscopy. *Annual review of biophysics and biophysical chemistry* **1988**, *17*, 145–166.

[9] Greenfield, N. J. Using circular dichroism spectra to estimate protein secondary structure. *Nature protocols* **2006**, *1*, 2876.

[10] Schnoering, G.; Poulikakos, L. V.; Rosales-Cabara, Y.; Canaguier-Durand, A.; Norris, D. J.; Genet, C. Three-Dimensional Enantiomeric Recognition of Optically Trapped Single Chiral Nanoparticles. *Phys. Rev. Lett.* **2018**, *121*, 023902.

[11] Narushima, T.; Okamoto, H. Circular dichroism nano-imaging of two-dimensional chiral metal nanostructures. *Phys. Chem. Chem. Phys.* **2013**, *15*, 13805–13809.

[12] Arteaga, O.; Sancho-Parramon, J.; Nichols, S.; Maoz, B. M.; Canillas, A.; Bosch, S.; Markovich, G.; Kahr, B. Relation between 2D/3D chirality and the appearance of chiroptical effects in real nanostructures. *Optics Express* **2016**, *24*, 2242–2252.

[13] García-Etxarri, A.; Dionne, J. A. Surface-enhanced circular dichroism spectroscopy mediated by nonchiral nanoantennas. *Physical Review B* **2013**, *87*, 235409.

[14] Kramer, C.; Schäferling, M.; Weiss, T.; Giessen, H.; Brixner, T. Analytic optimization of near-field optical chirality enhancement. *ACS photonics* **2017**, *4*, 396–406.

[15] Yamauchi, M.; Mawatari, K.; Hibara, A.; Tokeshi, M.; Kitamori, T. Circular dichroism thermal lens microscope for sensitive chiral analysis on microchip. *Analytical chemistry* **2006**, *78*, 2646–2650.

[16] Kong, X.-T.; Khosravi Khorashad, L.; Wang, Z.; Govorov, A. O. Photothermal Circular Dichroism Induced by Plasmon Resonances in Chiral Metamaterial Absorbers and Bolometers. *Nano Letters* **2018**, 2001–2008.

[17] Boyer, D.; Tamarat, P.; Maali, A.; Lounis, B.; Orrit, M. Photothermal imaging of nanometer-sized metal particles among scatterers. *Science* **2002**, *297*, 1160–1163.

[18] Berciaud, S.; Lasne, D.; Blab, G. A.; Cognet, L.; Lounis, B. Photothermal heterodyne imaging of individual metallic nanoparticles: Theory versus experiment. *Physical Review B* **2006**, *73*, 045424.

[19] Gaiduk, A.; Ruijgrok, P. V.; Yorulmaz, M.; Orrit, M. Detection limits in photothermal microscopy. *Chemical Science* **2010**, *1*, 343.

[20] Selmke, M.; Braun, M.; Cichos, F. Photothermal single-particle microscopy: detection of a nanolens. *ACS Nano* **2012**, *6*, 2741–2749.

[21] Yorulmaz, M.; Khatua, S.; Zijlstra, P.; Gaiduk, A.; Orrit, M. Luminescence quantum yield of single gold nanorods. *Nano Letters* **2012**, *12*, 4385–4391.

[22] Yorulmaz, M.; Nizzero, S.; Hoggard, A.; Wang, L.-Y.; Cai, Y.-Y.; Su, M.-N.; Chang, W.-S.; Link, S. Single-Particle Absorption Spectroscopy by Photothermal Contrast. *Nano Letters* **2015**, *15*, 3041–3047.

[23] Hou, L.; Adhikari, S.; Tian, Y.; Scheblykin, I. G.; Orrit, M. Absorption and quantum yield of single conjugated polymer poly [2-methoxy-5-(2-ethylhexyloxy)-1, 4-phenylenevinylene](MEH-PPV) molecules. *Nano Letters* **2017**, *17*, 1575–1581.

[24] Gaiduk, A.; Yorulmaz, M.; Ruijgrok, P. V.; Orrit, M. Room-Temperature Detection of a Single Molecule's Absorption by Photothermal Contrast. *Science* **2010**, *330*, 353–356.

[25] Kuwata-Gonokami, M.; Saito, N.; Ino, Y.; Kauranen, M.; Jefimovs, K.; Vallius, T.; Turunen, J.; Svirko, Y. Giant optical activity in quasi-two-dimensional planar nanostructures. *Physical Review Letters* **2005**, *95*, 227401.

[26] Vinegrad, E.; Vestler, D.; Ben-Moshe, A.; Barnea, A. R.; Markovich, G.; Cheshnovsky, O. Circular Dichroism of Single Particles. *ACS Photonics* **2018**, *5*, 2151–2159.

[27] Nechayev, S.; Barczyk, R.; Mick, U.; Banzer, P. Substrate-Induced Chirality in an Individual Nanostructure. *ACS Photonics* **2019**, *6*, 1876–1881.

[28] Jackson, J. D. *Classical electrodynamics*, 3rd ed.; John Wiley & Sons: New York, 1998.

[29] Karst, J.; Karst, J.; Cho, N. H.; Kim, H.; Lee, H.-E.; Nam, K. T.; Giessen, H.; Hentschel, M. Chiral Scatterometry on Chemically Synthesized Single Plasmonic Nanoparticles. *ACS Nano* **2019**, *13*, 8659–8668.

[30] Wang, L.-Y.; Smith, K. W.; Dominguez-Medina, S.; Moody, N.; Olson, J. M.; Zhang, H.; Chang, W.-S.; Kotov, N.; Link, S. Circular Differential Scattering of Single Chiral Self-Assembled Gold Nanorod Dimers. *ACS Photonics* **2015**, *2*, 1602–1610.

[31] Lumerical: Sources - TFSF. `https://kb.lumerical.com/ref_sim_obj_sources_tfsf.html`, Accessed: 2010-09-11.

[32] Lumerical: advanced spatial absorption. `https://kb.lumerical.com/layout_analysis_pabs_adv.html`, Accessed: 2010-08-16.

[33] Lumerical: Material Database. `https://kb.lumerical.com/materials_material_database_optical.html`, Accessed: 2010-09-11.

[34] Palik, E. D. *Handbook of optical constants of solids*; Academic press, 1998; Vol. 3.

[35] Kedenburg, S.; Vieweg, M.; Gissibl, T.; Giessen, H. Linear refractive index and absorption measurements of nonlinear optical liquids in the visible and near-infrared spectral region. *Optical Materials Express* **2012**, *2*, 1588–1611.

[36] van Aarle, W.; Palenstijn, W. J.; Beenhouwer, J. D.; Altantzis, T.; Bals, S.; Batenburg, K. J.; Sijbers, J. The ASTRA Toolbox: A platform for advanced algorithm development in electron tomography. *Ultramicroscopy* **2015**, *157*, 35 – 47.

[37] Baffou, G.; Berto, P.; Bermúdez Ureña, E.; Quidant, R.; Monneret, S.; Polleux, J.; Rigneault, H. Photoinduced heating of nanoparticle arrays. *Acs Nano* **2013**, *7*, 6478–6488.